JOC The Journal of Organic Chemistry

pubs.acs.org/joc Article

Theoretical Insights into [NHC]Au(I) Catalyzed Hydroalkoxylation of Allenes: A Unified Reaction Valley Approach Study

Małgorzata Z. Makoś, Marek Freindorf, Yunwen Tao, and Elfi Kraka*

Cite This: *J. Org. Chem.* 2021, 86, 5714−5726 Read Online

ACCESS | Metrics & More | Article Recommendations | Supporting Information

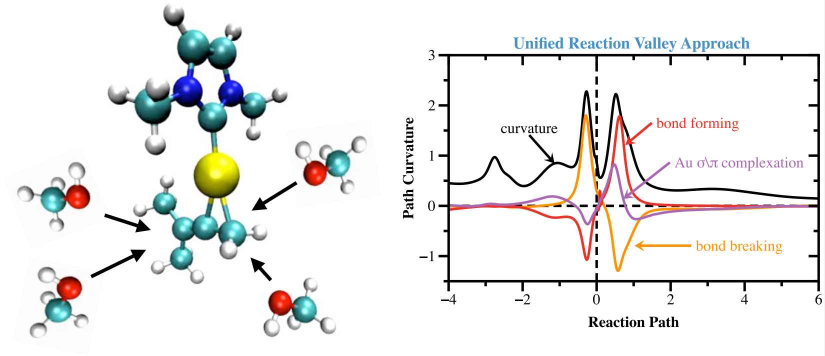

ABSTRACT: Hydroxylation is an effective approach for the synthesis of carbon−oxygen bonds and allylic ethers. The [NHC]Au(I) catalyzed intermolecular hydroalkoxylation of allene was studied at the DFT and Coupled Cluster level of theory. Using the Unified Reaction Valley Approach (URVA), we carry out a comprehensive mechanistic analysis of [NHC]Au(I)-catalyzed and noncatalyzed reactions. The URVA study of several possible reaction pathways reveal that the [NHC]Au(I) catalyst enables the hydroalkoxylation reaction to occur via a two step mechanism based upon the Au ability to switch between π- and σ-complexation. The first step of the mechanism involves the formation of a CO bond after the transition state with no energy penalty. Following the CO bond breakage, the OH bond breaks and CH bond forms during the second step of the mechanism, as the catalyst transforms into the more stable π−Au complex. The URVA results were complemented with local vibrational mode analysis to provide measures of intrinsic bond strength for Au(I)-allene interactions of all stationary points, and NBO analysis was applied in order to observe charge transfer events along the reaction pathway. Overall, the π−Au C═C interactions of the products are stronger than those of the reactants adding to their exothermicity. Our work on the hydroxylation of allene provides new insights for the design of effective reaction pathways to produce allylic ethers and also unravels new strategies to form C−O bonds by activation of C═C bonds.

■ INTRODUCTION

N-Heterocyclic carbene gold(I) complexes, [NHC]Au(I), have attracted lots of attention during the past two decades due to their excellent catalytic activity for various reactions including biological activities.[1−8] The NHC ligand provides electronic and steric stabilization,[9−11] making [NHC]Au(I) catalyst, in the case of nucleophilic addition, chemoselective toward the unsaturated carbon−carbon bond in alkynes, alkenes, and allenes.[12−16] For example, the hydroalkoxylation of allenes was shown to be an efficient reaction for the allylic ethers production as well as the C−O and C(sp^3)−C(sp^2) bond formation, gaining access to a wide variety of functionalized molecules.[17−19]

Allenes are commonly used in organic reactions due to their inherent flexibility and susceptibility to metal bonding,[20] making them attractive in modern chemistry as building blocks in synthesis, medical chemistry, and material science.[21,22] Widenhoefer and co-workers reported the first example of an [NHC]Au(I)-allene π complex.[23] Recently, his group focused on gaining kinetic and mechanistic insights into reactions involving allenes and alcohols using different gold catalyst transformations.[24] Paton and Maseras computationally investigated σ-coordinated Au(I) allenyl cation structures, where these structures were recognized as intermediates in the hydroalkoxylation of allenes reaction.[25] This triggered a number of experimental and computational reports of the functionalization of allenes with a variety of nucleophiles and metals, particularly hydration,[26,27] hydroamination,[28,29] and hydroalkoxylation,[21,30] where gold has been extensively investigated.[31−36] Although these studies were mostly focused

Received: January 27, 2021
Published: March 29, 2021

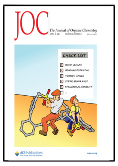

https://doi.org/10.1021/acs.joc.1c00208

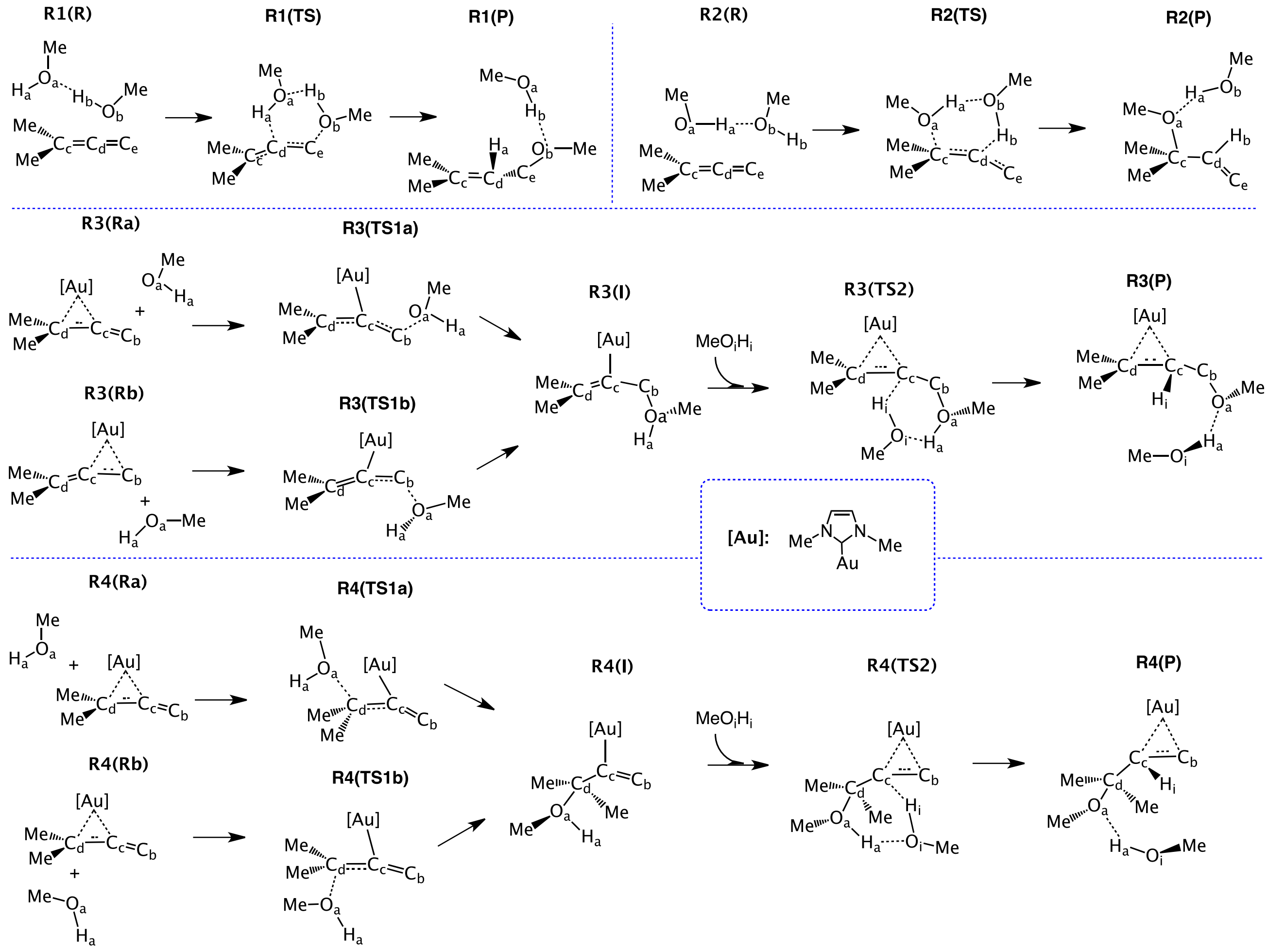

Figure 1. Noncatalyzed reactions **R1** and **R2**. [NHC]Au(I)-catalyzed reactions **R3** and **R4**, where the first step proceeds through the alternative pathways.

on kinetics, ligand efficiency, and reversibility aspects of the reactions, a complete account of the reaction mechanism of the hydroalkoxylation of allene is yet to be presented.

In this work, we provide an in-depth analysis of the reaction mechanism by bridging the mechanistic features of the reaction path with the insights provided by the local force constant, electron density distribution, and NBO analysis along the reaction path. For this purpose, we use the Unified Reaction Valley Approach (URVA)[37] to conduct a comprehensive study of the [NHC]Au(I)-catalyzed and noncatalyzed hydroalkoxylation of allenes. URVA is based on the fact that any change in the electronic structures of the reaction complex, including its vibrations, is related to the translational motion along the reaction path curvature. Hence, the analysis of the scalar curvature of the reaction path provides a direct insight into all chemical events occurring during a chemical reaction. A number of advantages of URVA include (1) identifying the regions of the potential energy surface (PES) that are directly related to chemical events such as bond-forming and breaking processes; (2) registering all changes in the reaction complex from the entrance to the exit channel (beyond those at the TS or stationary points); (3) analyzing the charge transfer and polarization along the reaction path; and (4) determining the reacting phases and their importance.[38−41] In this context, URVA was previously applied for an extensive study on the [NHC]Au(I) catalyzed [3,3]-sigmatropic rearrangement of allyl acetate.[37] Here, we used URVA to pursue the following objectives:

- To identify similarities and differences between the [NHC]Au(I)-catalyzed and the noncatalyzed reactions, and to determine the nature of the nucleophilic attack by a detailed analysis of the reaction path curvature and related features.
- To prove/disprove the current hypothesis that the reaction mechanism of the hydroalkoxylation of allene is always the same, i.e., independent of the approaching orientation of the alcohol.
- To identify the most energy-consuming contributions to the energy barrier.
- To quantify the intrinsic strength of the Au(I)-allene interactions and the C═C bonds of allene via a bond strength order (BSO*n*) parameter derived from local vibrational force constants for all stationary points.
- To monitor the C−O bond formation via the topological analysis of the electron density distribution along the reaction path.
- To monitor the charge transfer along the reaction path via NBO analysis.

As shown in Figure 1, nucleophile attacks allene from different approaching orientations, (i) alcohol is added to the terminal carbon atoms (called distal and proximal addition,[42] reactions **R1**, **R3** and **R2**, **R4**, respectively), and (ii) the attack

Table 1. Reaction Energetics (kcal/mol) for All Hydroalkoxylation of Allenes Studied in This Work[a]

		DFT		DLPNO−CCSD(T)					
react.	step	$\Delta E^{\#}$	ΔE_R	$\Delta E^{\#}$	ΔE_R	$\Delta H^{\#}$	ΔH_R	$\Delta G^{\#}$	ΔG_R
R1		39.5	−25.8	49.1	−22.1	45.1	−20.8	50.7	−17.2
R2		37.2	−24.2	45.6	−23.1	40.9	−22.5	47.1	−17.6
R3	1a	16.6	8.6	20.0	10.8	19.1	11.7	20.4	15.2
	1b	17.1	8.0	20.4	10.6	20.6	11.7	25.9	17.1
	2	3.0	−25.8	4.8	−26.7	2.6	−25.1	2.9	−25.3
R4	1a	14.1	7.2	16.3	7.8	15.1	8.3	16.7	12.9
	1b	11.8	11.1	15.4	13.7	15.2	14.4	19.4	19.1
	2	8.7	−22.5	10.4	−24.0	7.6	−22.8	7.6	−23.8

[a] Calculated at DFT: PBE0/6-31G(d,p)SDD(Au) and DLPNO−CCSD(T)/def2-QZVPP/def2-QZVPP/C (Au) activation energies ($\Delta E^{\#}$), enthalpies ($\Delta H^{\#}$), and Gibbs free energies ($\Delta G^{\#}$); reaction energies (ΔE_R), enthalpies (ΔH_R), and Gibbs free energies (ΔG_R). For coupled cluster enthalpies and Gibbs free energies, the DFT thermochemistry was used.

occurs from the same side as a coordinated catalyst or from the opposite side (called inner- and outer-sphere mechanism,[25] step 1a and 1b of **R3** and **R4**, respectively). The alternative approaching orientations lead to stereoisomers of the σ-Au(I) allenyl intermediate (e.g., the intermediate of step 1a and step 1b), while the allylic ether product is obtained in the second step, after the addition of the second methanol unit and final isomerization.

RESULTS AND DISCUSSION

Reaction Energetics. Table 1 presents the energies of the reactions **R1**−**R4** based on DLPNO−CCSD(T) and DFT calculations, while Figure 2 presents the energy profiles based on DFT calculations. As shown in Table 1, for the first endothermic step of the catalytic reactions, the activation energy is 2.2−3.6 kcal/mol lower at the DFT level of theory than at the DLPNO−CCSD(T). For the second exothermic step, DFT barriers are 1.8 kcal/mol lower than the corresponding energies of DLPNO−CCSD(T). Generally, DFT overestimates the effect of electron correlation, especially in the case of the transition state (TS), which usually leads to a lower barrier.[43] However, the dual-level approach confirmed that DFT correctly reproduces the general trends for reactions **R1**−**R4**, and the discussion below is based on DFT energetics.

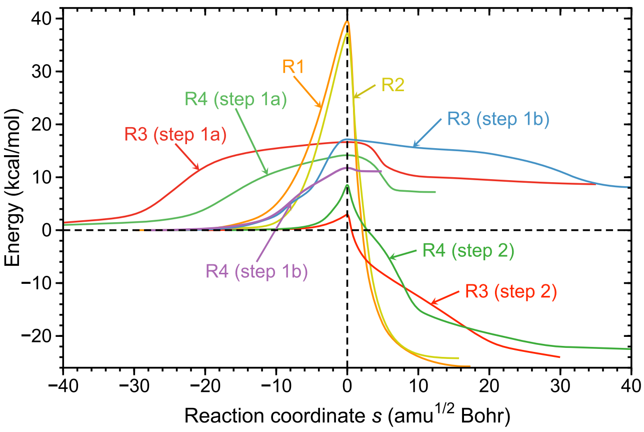

Figure 2. Energy profiles of the hydroalkoxylation of allene: the noncatalyzed (**R1** and **R2**) and [NHC]Au(I)-catalyzed reactions (**R3** and **R4**). PBE0/6-31G(d,p)SDD(Au) calculations. Figure cropped at $s = 40$ amu$^{1/2}$ Bohr. The energy profiles of all reactions are presented in Figure S1−S8 of Supporting Information.

The noncatalyzed reactions, **R1** and **R2**, where the nucleophile directly attacks the C═C bond, are exothermic and proceed in one step with an activation energy of 39.5 and 37.2 kcal/mol, respectively (see Table 1). Such a high barrier suggests that the noncatalyzed reaction will not occur under normal conditions. As shown in Figure 1, the [NHC]Au(I) catalyzed reactions, **R3** and **R4**, proceed in two steps, which is in agreement with other studies.[25,37,44] The high carbophilicity of the [NHC]Au(I) catalyst contributes to the formation of a π−Au(I) allene complex, thus favorably lowering the barrier of the first step to a range of 11.8−17.1 kcal/mol, leading to a σ-Au(I) allenyl intermediate. The difference in energy barrier height is due to the different coordination of the alcohol units. Activation energies in reactions **R4** are lower than those in **R3** because alcohol addition in **R4** takes place on the most substituted carbon atom.[25,27] The σ-Au(I) allenyl intermediate of the reactions **R3a/b** and **R4a/b** are regioisomers with the energies of 8.0−8.6 kcal/mol and 7.2−11.1 kcal/mol, relative to the starting structures. The resulting intermediates are less stable than the starting π−Au(I) structures, which is in line with previous studies.[37]

The barrier height is determined to a great extent by chemical events happening in the entrance channel. As shown in Figure 2, the noncatalyzed reactions are characterized by a shorter entrance channel, and the energy barrier increases when the reaction complex is closer to the TS. Meanwhile, in the first step of the catalyzed reactions, the energy increases slowly through the long entrance channel (see Figure S1−S8), suggesting it is a rate-determining step. Furthermore, steps 1a and 1b of **R3** are characterized by a significantly longer exit channel when compared to **R4** ($s = 35−40$ vs $s = 7−15$ amu$^{1/2}$ Bohr; see Figure 2), as an additional phase might be needed for the conformational adjustment of [NHC]Au(I) catalyst and allene or the finalization of the CO bond formation in distal addition of alcohol. In the second step, the σ bond is cleaved, and Au(I) is coordinated to the allylic ether products via π-bond, which requires a small energy barrier of only 3.0 and 8.7 kcal/mol. The π−Au(I) allylic ether products are located as much as 25.8 kcal/mol below the starting structures, suggesting that these reactions are irreversible.

In summary, the lowering of the activation energy by even 27.7 kcal/mol compared with noncatalyzed reaction reflects the catalytic power of the [NHC]Au(I) catalyst. However, calculated energetics allows us to test only the overall performance of the noncatalyzed and Au(I)-catalyzed reactions. A thorough analysis of the most significant features for

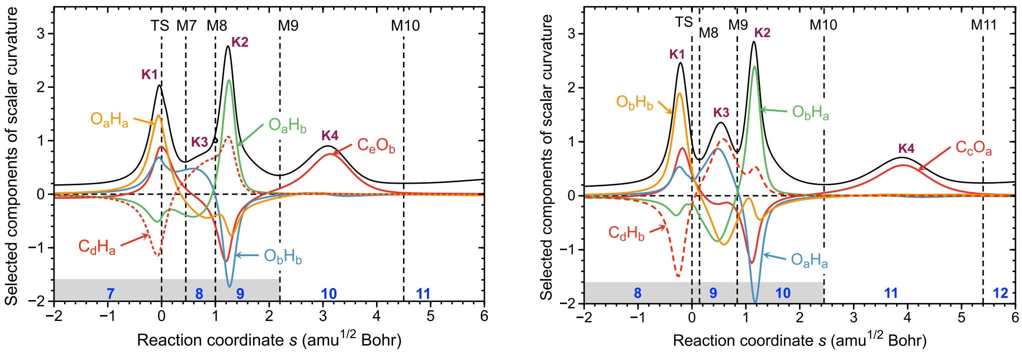

(a) Reaction **R1** (b) Reaction **R2**

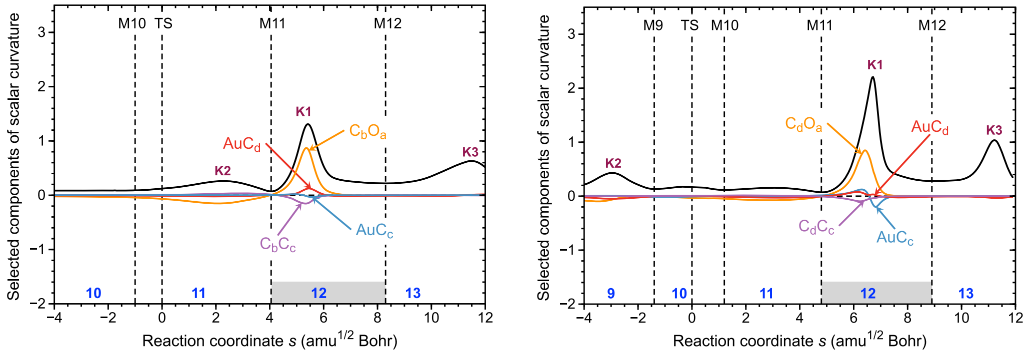

(c) Reaction **R3** step 1a (d) Reaction **R4** step 1a

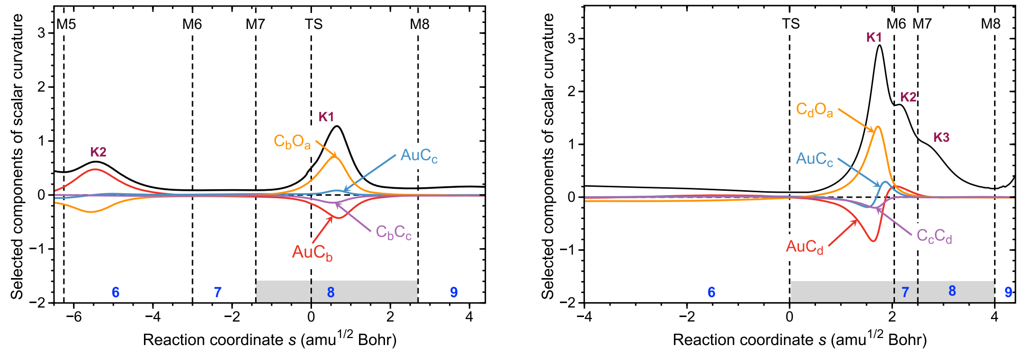

(e) Reaction **R3** step 1b (f) Reaction **R4** step 1b

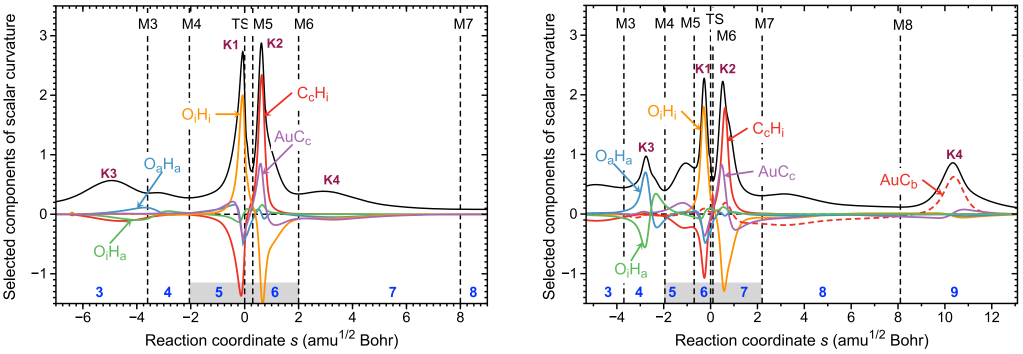

(g) Reaction **R3** step 2 (h) Reaction **R4** step 2

Figure 3. Scalar curvature as a function of the reaction path parameter s (solid black line) of the hydroalkoxylation of allenes. The decomposition of the scalar curvature into the most important bond components is given in colors. Vertical dashed lines at the curvature minima M1, M2, etc., show the borders of the reaction phases and the transition state (TS) at $s = 0$ amu$^{1/2}$ Bohr. K1, K2, etc., are the curvature maxima. The reaction phases are denoted in blue. The range of the reaction path is narrowed down to show only the chemical phases (gray bar), for a full reaction path, see Figures S1−S8 of the Supporting Information. For numbering of the atoms, see Figure 1.

the **R1**−**R4** reaction mechanisms based on the features of the reaction valley is provided below.

Curvature Profiles, Reaction Mechanism. In order to quantify the mechanism of the reactions, the analysis of the reaction path curvature and its decomposition into internal coordinate components is presented in the following. The curvature profiles of reactions **R1**−**R4** are discussed with a focus on elucidating the mechanistic differences between noncatalyzed and [NHC]Au(I)-catalyzed reactions including difference of Au-catalyst and alcohol orientations. Figure 3 presents the curvature profiles of the chemical phases. The Supporting Information presents the complete curvature profiles and corresponding energy profiles in Figures S1−S8, and Supporting Videos showing the evaluation of the reaction complexes along the reaction path.

Noncatalyzed Reactions. The prechemical phases of the reactions **R1** and **R2** stretch for over 25 *s*-units (see Figure S1 and S2), in which conformational changes prepare the molecule for the reaction, i.e., almost the entire entrance channel is needed for the reactant to prepare before the actual chemical processes take place in the phases of close proximity to the transition state (TS). In these two reactions, the main peak K1 (shortly before TS) is related to the cleavage of alcohol's OH bond (O_aH_a in **R1** and O_bH_b in **R2**, orange line) and the coordination of hydrogen to allene's C_d-central atom. The curvature components in K1 related to the C−H bond formation (C_dH_a in **R1** and C_dH_b in **R2**, dashed red line) are negative, thus indicating that the reactant defies the C−H bond formation, and energy is needed to overcome this resistance. As a result, in **R1**, the energy increases by 21.9 kcal/mol in the phase before TS, which is 60% of the energy barrier (see Table 2 and Table S1). The energy decreases shortly after the TS, leading to increasing steric hindrance, which is characterized by the curvature enhancement K3.

Table 2. Energy Contribution (kcal/mol) of Each Reaction Phase to the Reaction Barrier[a]

R1			R3 step 1b			R3 step 2		
phase	E_p	E_c	phase	E_p	E_c	phase	E_p	E_c
1	0	0	1	0	0	1	0	0
2	0	0	2	0.3	0.3	2	0	0
3	0	0	3	0.9	1.2	3	0.6	0.6
4	0.4	0.4	4	3.1	4.3	4	0.6	1.2
5	8.9	9.3	5	2.3	6.6	5	1.9	3.1[b]
6	21.9	31.2	6	6.1	12.7			
7	8.3	39.5[b]	7	3.7	16.4			
			8	0.8	17.2[b]			

[a] E_p energy contribution to the reaction phase. E_c cumulative energy at the end of the reaction phase. Calculated at PBE0/6-31G(d,p)/SDD(Au). For the energy contribution to all reactions **R1**−**R4**, see Table S1 in Supporting Information. [b] The TS energy contained in this phase.

Newly generated coordination vacancy at the alcohol unit gives the onset of formation of a new O−H bond (O_aH_b in **R1** and O_bH_a in **R2**), which has a positive contribution to the curvature peak and hence supporting the bond formation (green line). In the chemical phases (gray bar in Figure 3a and 3b), the electron density of the C−C bond (C_dC_e in **R1** and C_cC_d in **R2**) is delocalized, which is essential for the formation of a C−O bond. The C−O curvature components (C_eO_b in **R1** and C_cO_a in **R2**, solid red line) change from supporting (i.e., positive) contributions in K1 to resisting (i.e., negative) in K3 and K2, extending further to the peak K4. This displacement is related to the polarization of the CC bond by approaching alcohol, and consequently, we can observe that the van der Waals complex converts into the covalently bonded product, which adopts its equilibrium geometry in the 15 *s*-units long postchemical stage.

Au(I)-Catalyzed Reactions. The curvature profiles of the [NHC]Au(I)-catalyzed reactions **R3** and **R4** of hydroalkoxylation of allene are presented in Figure 3c−h. Reaction R3 is a distal reaction in which the alcohol attacks the terminal C_b-atom with two hydrogens. In contrast, **R4** represents a proximal reaction, because the alcohol is added to the C_d-atom with two methyl groups (i.e., the most substituted carbon). Au(I) also prefers to bond to C_d, while having π interactions with C_c−C_d. Only in **R3(Rb)**, Au(I) bonds to the C_b−C_c (see Figure 1), as the different catalyst positions relative to the allene are known in the literature.[13,42] The prechemical phases of step 1a of **R3** and **R4** encompass over 55 *s*-units (see Figures S3 and S6), caused by the inner-sphere mechanism, where the addition of alcohol comes from the same side as the catalyst. Those prechemical phases feature the rotation of the [NHC]Au(I) by driving apart the [NHC] ligand and allene methyl groups, creating a channel for the nucleophile, which gradually increases the energy barrier (as shown in Table S1). Step 1b of **R3** and **R4** presents the outer-sphere mechanism, in which the addition of alcohol comes from the opposite side as the catalyst, the prechemical phases are shorter, stretching for almost 25 *s*-units (see Figures S4 and S7).

The main characteristic of the curvature profile of the first step is distinguished by a peak K1 appearing after the TS. Peak K1 is related to the CO bond formation and takes place from 1.5 to 7 *s* units after the TS, depending on the coordination of catalysts or alcohol orientation, confirming that the bond breaking/forming processes do not necessarily happen at the TS.[41,45] During the formation of the C−O bond, the terminal C atom hybridizes to sp^3 and accepts the electron density from the alcohol, which can be observed by the positive curvature component in K1 (Figure 3c−f, orange line). The K1 peak in step 1a of **R3** and **R4** are relatively narrow, which is typical when many minor geometrical adjustments collectively prepare the system for the bond formation. Hence, small contributions to the K1 are observed when the allene tilts from a π toward σ interactions with the Au(I)-catalyst (red and blue lines in Figure 3c,d). Breaking π−Au(I) C−C interactions contributes to the reaction curvature only in step 1b of reactions **R3** and **R4** (red line, Figure 3e,f). In the former, a small curvature peak K2 appears before the TS as the system has to synchronize the Au(I)-catalyst and alcohol rotations (Figure 3e). This additional maneuver adds 6.1 kcal/mol to the energy barrier (see Table 2), reflecting the most energy-consuming phase in this reaction. Contrary, in reaction **R4** step 1b, breaking the π Au−C interactions happens after the TS, which does not affect the energy barrier; however, it leads to the relatively large resisting (i.e., negative) curvature component at K1 (Figure 3f, red line). A narrow and high peak K1 at the end of the reaction path, implying the CO bond requires even less preparation and occurs rapidly, which is reflected by the lowest energy barrier and shortest exit channel comparing to other reactions. Since the formation of σ-bonded Au(I) intermediate is endothermic by 7.2−11.1 kcal/mol, the regeneration of a stable π−Au(I) complex continues in step 2, establishing the new C_cH_i bond, which simultaneously weakens and breaks the O_iH_i bond

Table 3. Summary of Geometric, Electronic, and Vibrational Data of the Stationary Points of R1 and R3 (Step 1a, Step 2)[a]

complex	bond	r	k^a	ω^a	BSO*n*	$\rho(\mathbf{r}_c)$	$H(\mathbf{r}_c)$
R1(R)	C_cC_d	1.311	10.347	1710.9	2.03	0.348	−0.427
	C_dC_e	1.311	10.455	1719.8	2.04	0.345	−0.428
	C_eO_b	3.317	0.087	146.9	0.06		
	C_cC_d	1.338	9.070	1601.8	1.82	0.331	−0.364
R1(TS)	C_dC_e	1.399	5.513	1248.8	1.20	0.305	−0.319
	C_eO_b	1.847	0.701	416.5	0.24	0.096	−0.029
	C_cC_d	1.341	9.418	1632.2	1.87	0.339	−0.376
R1(P)	C_dC_e	1.496	4.524	1131.3	1.02	0.263	−0.225
	C_eO_b	1.427	4.424	1046.5	0.88	0.252	−0.357
	AuC_c	2.313	0.685	320.6	0.65	0.091	−0.030
	AuC_d	2.199	0.875	362.4	0.74		
R3(Ra)	C_cC_d	1.359	7.898	1494.7	1.62	0.326	−0.355
	C_bC_c	1.313	10.152	1694.6	1.99	0.344	−0.440
	C_bO_a	3.305	0.079	139.5	0.05		
	AuC_c	2.073	2.048	554.3	1.20	0.126	−0.056
	AuC_d	3.071	0.850	357.2	0.73		
R3(TS1a)	C_cC_d	1.393	6.024	1305.4	1.30	0.313	−0.323
	C_bC_c	1.387	5.003	1189.6	1.11	0.316	−0.334
	C_bO_a	2.267	0.063	124.9	0.04	0.038	−0.002
	AuC_c	2.065	2.291	586.4	1.28	0.131	−0.060
	AuC_d	3.031	1.049	396.7	0.82		
R3(I)	C_cC_d	1.358	8.431	1544.3	1.71	0.328	−0.354
	C_bC_c	1.496	4.238	1094.9	0.97	0.261	−0.230
	C_bO_a	1.484	2.572	798.0	0.60	0.207	−0.266
	AuC_c	2.113	1.857	527.9	1.14	0.114	−0.048
	AuC_d	3.032	0.755	336.7	0.68		
	C_cC_d	1.366	7.816	1487.0	1.61	0.325	−0.348
R3(TS2)	C_bC_c	1.515	4.104	1077.4	0.94	0.254	−0.212
	C_bO_a	1.439	4.124	1010.4	0.84	0.241	−0.339
	AuC_c	2.236	1.015	390.2	0.81	0.085	−0.026
	AuC_d	2.337	0.626	306.5	0.62		
R3(P)	C_cC_d	1.386	7.327	1439.7	1.52	0.316	−0.324
	C_bC_c	1.502	4.514	1129.9	1.02	0.261	−0.222
	C_bO_a	1.411	4.900	1101.3	0.95	0.263	−0.387

[a] Calculated at PBE0/6-31G(d,p)/SDD(Au), bond length r [Å], local mode force constant, k^a [mdyn/Å], local modes frequencies ω^a [cm^{-1}], bond strength order BSO*n*, electron density $\rho(\mathbf{r}_c)$ [e/$Bohr^3$], and energy density $H(\mathbf{r}_c)$ [Hartree/$Bohr^3$] at the bond critical point $\mathbf{r}_c$. For all complexes, see Table S2 in Supporting Information. For numbering of atoms, see Figure 1.

represented by a sharp curvature peaks K1 and K2 in a close proximity to the TS (Figures 3g and 3h). Peak K3 related to an adjustment and H_a migration between the alcohol groups has a stronger contribution in the case of **R4**, thus leading to a relatively higher barrier when comparing to **R3** step 2. The reaction ends with the formation of an Au(I) *π*-complex, which starts with a relatively small supporting (i.e., positive) contribution of AuC_c interactions to the K2. However, only in **R4**, peak K4 reflects the positive contributions of *π* Au−C_b bond (Figure 3h, broken red line). The reaction ends with the formation of an Au(I)-allylic ether *π*-complex, which stretches over the entire exit channel characterized by small, energy-saving pseudorotations of the allylic ether product and adjustments of the [NHC] ligand.

In summary, URVA confirms the split of the hydroalkoxylation into two energetically favorable steps by the [NHC]Au(I) catalyst, which is in line with other studies.[25,37,44] Additionally, URVA reveals that in the reaction process, the formation of the CO bond takes precedence, while the H-migration is shifted to the second step. This is rationalized by the preference of alcohol for terminal carbon sp^3 hybridization, which is possible on the opening of the double bond. The [NHC]Au(I) catalysis converts both central and terminal C atoms from sp^2 to sp^3 hybridization, which stabilizes the primary product, lowers the energy barrier, and therefore accelerates the reaction. The preference for carbon sp^3 hybridization is also expressed by lower force constants of the CC bond in the reactant of catalyzed reactions, which is explained in detail in the following section.

Bond Strength Orders. To understand the nature of the *π*- and *σ*-Au(I) interactions with C═C bond, we applied the local mode analysis[46] for all Au(I)-catalysis reactants (allene and alcohol), intermediates (allenyl) and products (allylic ether) complemented by the topological analysis of the electron density distribution $\rho(\mathbf{r})$.[47] In order to examine the covalent or electrostatic character of the Au−C and C−C bonds, we applied the Cremer−Kraka criterion, which requests a negative, i.e., stabilizing local energy density, $H(\mathbf{r}_c)$, at the bond critical point, $\mathbf{r}_c$, for a covalent bond between two atoms whereas a positive, i.e., depleting $H(\mathbf{r}_c)$ indicating electrostatic interactions.[48,49] Properties related to the most relevant interactions for the reactions **R1** and **R3** (step 1a and 2), are given in Table 3. The corresponding data for all the reactions

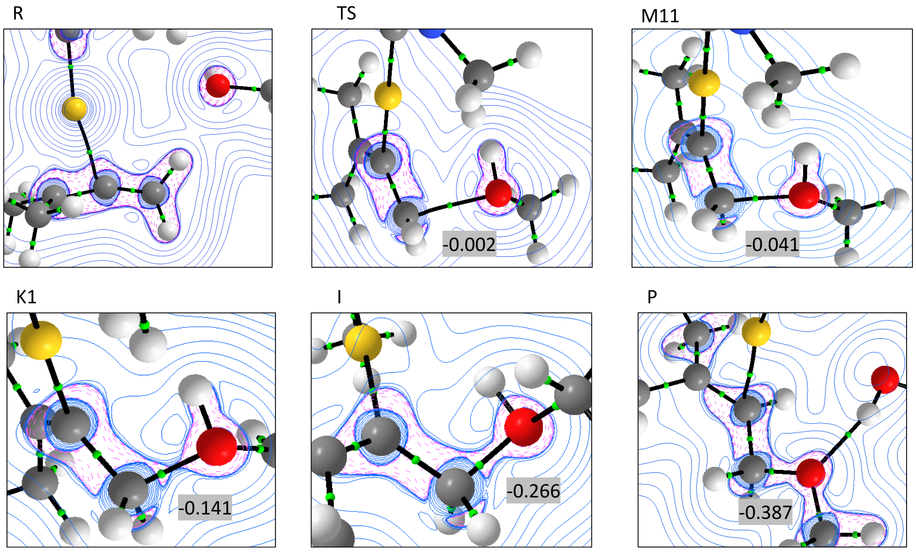

Figure 4. Laplacian contour plots of selected curvature points of the reaction **R3** step 1a. R, reactant; TS, transition state; M11, curvature minimum; K1, curvature peak; I, intermediate; and P, product (of step 2) plotted in the molecular plane. The dashed (pink) contours represent regions of charge concentration where $\nabla^2\rho(\mathbf{r}_c) < 0$, while the solid (blue) contours represent regions of charge depletion where $\nabla^2\rho(\mathbf{r}_c) > 0$. Numbers in gray boxes represent the energy density $H(\mathbf{r}_c)$ [Hartree/Bohr^3] at the bond critical point $\mathbf{r}_c$ (green dot). For the curvature points refer to Figure 3c.

R1−**R4** are provided in Table S2 in the Supporting Information.

The Au−C Interactions. During the reaction, the gold center changes its interactions with allene. The first step of the reaction is characterized by the π-bonded Au−C−C unit, which destabilizes the allene by pushing the electron density away from the C−C bond. The gold atom is oriented in the same plane as allene (see Figure 4, point R), forming a 35° C_c−Au−C_d angle and the distances between Au and C_cC_d are 2.313 and 2.199 Å, respectively. Despite the fact that Au is closer to terminal C_d, the BSO*n* is larger for center C_c (0.65 versus 0.74), and a bond critical point, $\mathbf{r}_c$, was found only at the AuC_c bond path, reflecting weak interaction by the $H(\mathbf{r}_c)$ of −0.030 hartree/Bohr^3. Reported values here correspond to the **R3(Ra)** complex; however, we observe the same peculiar phenomenon in all reactions (see Table S2). In these π-complexes, commonly only one bond path is found instead of two Au−C paths forming a three-membered ring.[37,50]

Accepting the electron density from the nucleophilic attack builds up the Au−C_c electron density, which leads to a weak covalent bond with $H(\mathbf{r}_c)$ of −0.060 hartree/Bohr^3, and the σ gold-allenyl complex is generated. Increasing C_c−Au−C_d angle drives the [NHC]Au out of the allene's plane so that the intermediate adopts an energetically less favorable conformation (8.6 kcal/mol above the starting structures). Formation of C_c−H_i bond labilizes the Au−C_c σ-bond and facilitates conversion into a π-complex. At the product **R3(P)**, the BSO*n* between Au and C_d and C_c are 0.81 and 0.62, respectively. As in the reactant, no 3-membered ring was found; only one bond path with a bond critical point is found for AuC_c with $H(\mathbf{r}_c)$ of −0.026 hartree/Bohr^3. Overall, the π−Au C−C interactions of the products are stronger than those for the reactants. On average, the BSO values of the products are 0.02 and 0.05 higher than in the reactants of **R3** and **R4**, respectively (see Table S2). In general, the stronger the bond formed, the more energy is released during the bond formation process. In the second step of reactions **R3** and **R4**, Au forms π-interactions with C−C, releasing more energy than needed to break the original π−Au C−C interactions in the first step. Stronger π−Au C−C interactions add to the exothermicity; however, they are not the main reason for lowering the enthalpy. During step 2, the C−H bond is also formed and C−O bonds is strengthened; therefore, the resulting system has lower energy than the reactants (see Table 1).

The C−O and C−C Bonds. Both CC bonds of allenes have an expected BSO*n* value of over 2, indicating the double bonding. Breaking a π-stabilization of allene by [NHC]Au(I) catalyst is reflected by smaller values of the BSO*n*; for example, in the **R3(Ra)**, the C_cC_d bond has a BSO*n* of 1.62. The **R3(TS1a)** marks the addition of the first alcohol unit. The distance between the C_b and O_a atoms shortens as the nucleophilic attack begins, which is indicated by the bond path made of a mixture of covalent and electrostatic interactions ($H(\mathbf{r}_c) \approx 0.0$, see Figure 4 point TS). Using the local concentration and depletion of charge described by the Laplacian of the electron density $\nabla^2\rho(\mathbf{r}_c)$, we observe that the electron density changes connected with a CO bond formation occurs in the vicinity of the corresponding curvature peak.[51] The overlap in the charge concentration initiating the C_bO_a bond formation results in the electron density accumulation between the C_bO_a atomic basins, consequently leading to the curving of the reaction path and curvature peak K1 (Figure 4, point K1). Further evaluation of the C_bO_a bond at the intermediate **R3(I)** shows a stronger bond with the BSO*n* of 0.95. Subsequently, the covalent character of the C_bO_a bond improves as viewed in the decrease of negative $H(\mathbf{r}_c)$ of −0.226 hartree/Bohr^3 values, while the electron density marks the transition of the shared-shell atomic basins to closed-shell atomic basins (Figure 4, point I). During the second step, the C_cC_d becomes weaker, with a BSO*n* of 1.6, supporting the π-bond between Au and the C_cC_d.

The strength of the CO bond is crucial for the final isomerization. Figure 5 shows that the CO bond is stronger in the final product **R3(P)** than in **R4(P)**. The BSO*n* values are 0.95 and 0.84, respectively. Similarly, in noncatalyzed reactions the CO bond is stronger in **R1(P)** than in **R2(P)** (BSO*n* 0.88

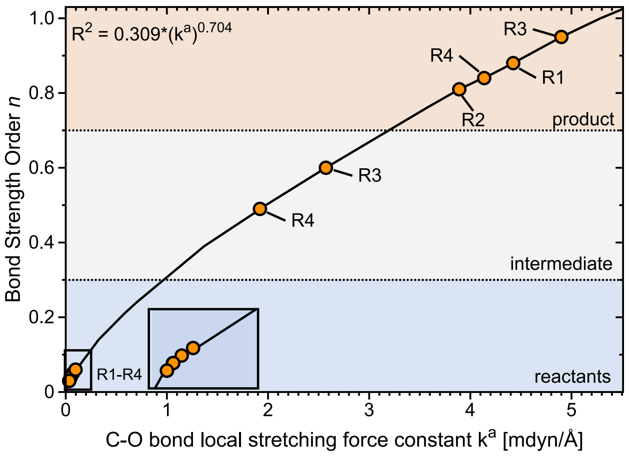

Figure 5. Power relationship between the BSOn and k^a values for CO bond in reactions **R1**−**R4**.

vs 0.81). This is related to the fact that in reactions **R1** and **R3** the nucleophilic attack takes place at less substituted C atom (with initially two H atoms); therefore, the strengthening of the CO bond stabilizes the final product. Consequently, the final products **R1(P)** and **R3(P)** are lower in energy than **R2(P)** and **R4(P)**, respectively.

Charge Transfer and Polarization along the Reaction Path. In the following section, we discuss the total charge transfer and charge polarization along the reaction path. The NBO charges along the reaction path are presented in Figures 6 and 7. The NBO charges of individual atoms at the stationary points of each reaction are shown in Figure S9 in the Supporting Information.

Because the oxygen atom of the alcohol group has an electron-withdrawing character and larger electronegativity, it polarizes the allene as it gets closer; therefore, the major difference in the Au(I)-catalyzed and noncatalyzed reactions results from the manner and magnitude of charge transfer. At the beginning of the noncatalyzed reactions, the total charge of the reaction complex is close to zero; however, as the reaction proceeds the charge separation increases (Figure 7a). The most changes are observed in the chemical phases (gray bar in Figure 6a). Atoms of newly created C_dH_a bond decrease their charges from +0.039 to −0.399 e and from +0.507 to +0.255 e, respectively, pushing the electron density toward terminal C_dC_e bond polarizing it and preparing for a C_eO_b bond formation. Consequently, C_e and O_b atoms increase their

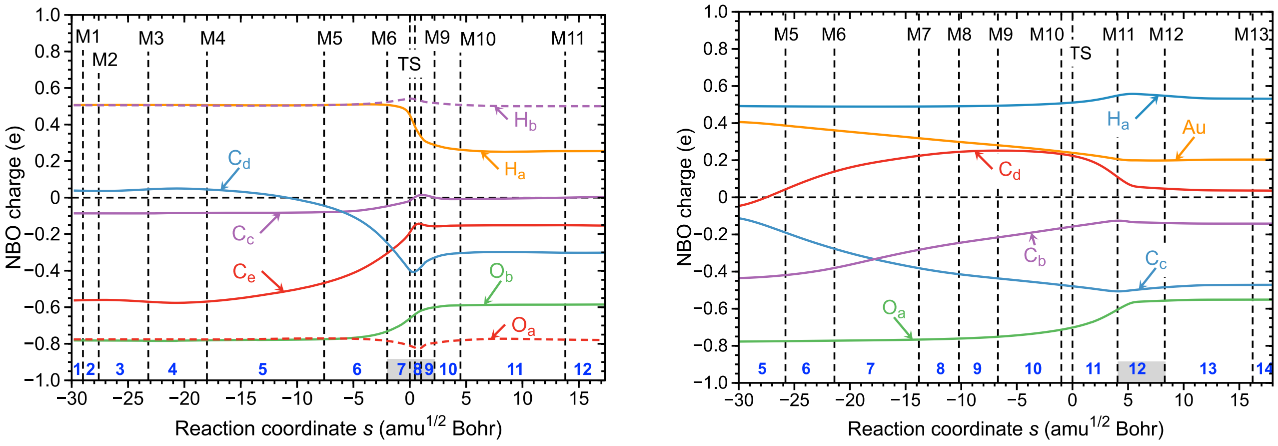

(a) Reaction **R1**

(b) Reaction **R3**, step 1a

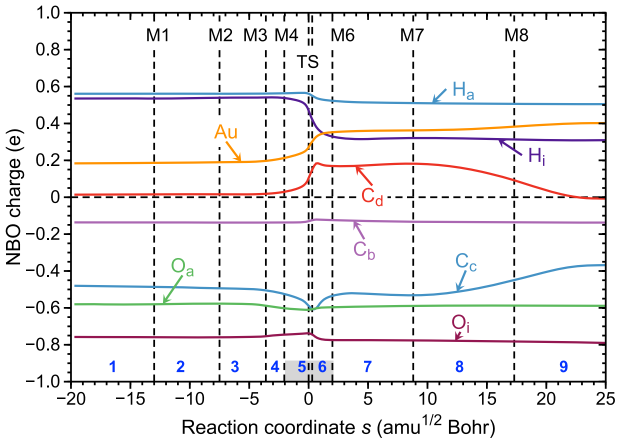

(c) Reaction **R3**, step 2

Figure 6. NBO charges along the reaction path as a function of the reaction coordinate s. The transition state (TS) at s = 0 amu$^{1/2}$ Bohr and the minima of the curvature profile M1, M2, ..., Mn are indicated by vertical black dashed lines. For numbering of atoms, see Figure 1.

https://doi.org/10.1021/acs.joc.1c00208
J. Org. Chem. 2021, 86, 5714−5726

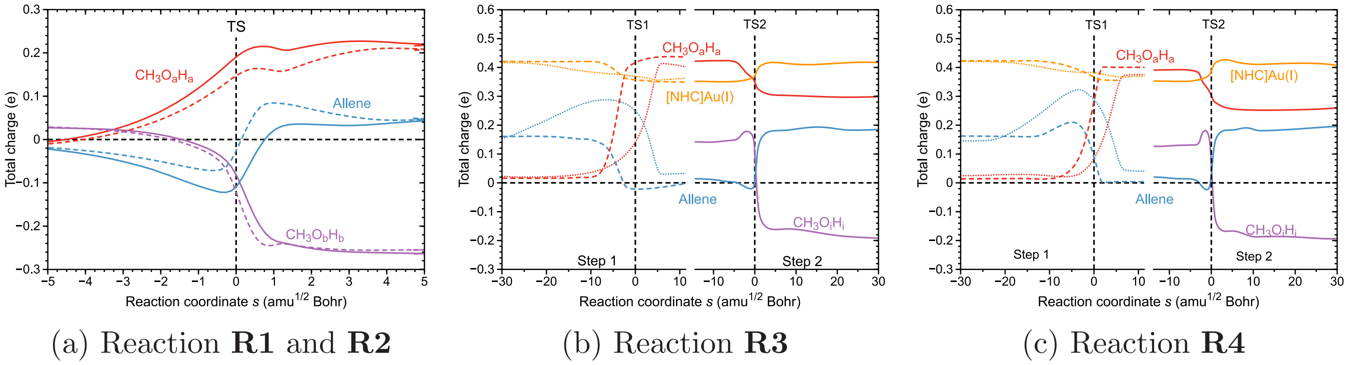

(a) Reaction **R1** and **R2**

(b) Reaction **R3**

(c) Reaction **R4**

Figure 7. Total NBO charges along the reaction path. The transition state at $s = 0$ amu$^{1/2}$ Bohr is indicated by a vertical black dashed line. (a) Reaction **R1** solid line, reaction **R2** dashed line, (b) Reaction **R3**, and (c) Reaction **R4**: step 1a dotted line, step 1b dashed line, and step 2 solid line.

charges from −0.563 to −0.155 e and from −0.782 to −0.585 e, respectively. Overall, we can observe a total charge continuously growing along the reaction path, starting from the beginning of the entrance channel.

Contrary to the noncatalyzed reactions, in the [NHC]Au(I)-catalyzed reactions, a small charge separation is observed at the TS. In **R3**, Au loses 0.166 e of the charge during the development of σ-bond with central C_c atom decreases charges from −0.113 to −0.479 e as the electron density transfers to the terminal C atoms. The C_d and C_b increase charges from −0.046 to +0.224 e and −0.435 to −0.157 e, respectively (Figure 6b), in preparation for the sp^2/sp^3 hybridization. The addition of the second alcohol unit during step 2 increases a total charge of allene. The transformation to the Au(I)-π complex contributes to accumulation of the electron density in the Au−C_d region as both atoms increase their charges. Au(I) gains up to +0.402 e and C_d up to +0.180 e in the presence of peak K2 in phase 6.

In the Au-catalyzed reaction, a strong and rapid polarization of the terminal C atom takes place, which is quantitatively reflected by the CO curvature component (orange line in Figure 3c−f). Despite the mechanistic similarity of **R3** and **R4**, each of the first steps can be electronically distinguished from the others. In step 1a, the polarization of the allene unit is delayed due to the steric repulsions between [NHC]Au and the incoming alcohol unit resulting in curvature peak K1 which is around 6 *s*-units behind the TS (phase 12, Figure 3e,f). In step 1b, the initial lone pair of oxygen smoothly approaches carbon, which results in no delay in polarization, and peak K1 and TS are in the same phase. Another distinct difference between **R3** and **R4** is the initial charges of the terminal carbon atoms. The carbon under the nucleophilic attack is more negatively charged in **R3** rather than in **R4** (−0.435 and −0.572 e vs −0.044 and −0.026 e, respectively). In the **R4**, the terminal C_d atom has already attached two methyl groups, implying that the appropriate orientation of the C_d π orbitals is achieved, which facilitates the nucleophilic attack of alcohol on C_d. Consequently, the activation energy of steps 1a and 1b in **R4** is lower than in **R3**. One may consider this conclusion to be trivial and to be derived from the charge distribution along the reaction path. However, there is no effective measure that clarifies when the charge changes are sufficient to start with a nucleophilic attack. This distinction is directly provided by the curvature component analysis available only through the Unified Reaction Valley Approach.

■ CONCLUSION

In this work, we shed important light on the mechanism of the hydroalkoxylation of allene in the presence of the [NHC]Au(I)-catalyst. The Unified Reaction Valley Approach (URVA) study was used to analyze in detail Au(I)-catalyzed and noncatalyzed reactions considering different coordinations of the nucleophilic attack. URVA reveals that gold breaks the reaction into two energetically favorable steps, characterizing the following features:

- In the noncatalyzed reaction, the nucleophilic attack requires a higher barrier as the strong CC bonds of allene first need to be destabilized by interactions from migrating hydrogen atoms; hence, the formation of the CO bond between alcohol and allene is spread through the chemical phases. In the presence of [NHC]Au(I) catalyst, the π-stabilizing effect of the allene is weakened; hence, the terminal C atom is prone to the sp^3 hybridization, the reaction is divided into two steps, and the activation energy is greatly reduced. The reaction path curvatures prove that the CO bond formation in the first step does not require additional energy so that the cleavage of OH bonds and the formation of CH bonds are transferred to the second step.
- By taking into account different approaching orientations of the alcohol in regard to the allene or Au(I)-catalyst, we noted subtle differences in the reaction mechanisms, especially in the first step. In the case of the inner-sphere mechanism, the CO bond formation is delayed due to the steric repulsions between [NHC]Au and the incoming alcohol unit, which is characterized by a late curvature peak. The outer-sphere mechanism requires even less preparation, and CO bond formation occurs rapidly in the same chemical phase as the TS. The differences in the second step are related to the distal or proximal addition of the nucleophile, as the steric repulsion is observed in proximal addition. However, considering the first step as rate-determining, the most favorable pathway is an outer-sphere-proximal mechanism.
- The local mode analysis of the CC, CO bonds, and Au−C interactions calculated for all stationary points complement the curvature data. The BSO*n* value indicates that the CO bond is stronger when alcohol attacks the less substituted carbon, which is rationalized

by the electron density transfer between the Au(I)-catalyst, allene, and the alcohol unit. A stronger CO bond also contributes to the more stable product.

- The driving force behind these reactions is the charge transfer between Au-catalyst, allene, and alcohol. In noncatalyzed reactions, there is a maximum charge separation at the TS between allene and the alcohol unit. However, in the [NHC]Au(I)-catalyzed reaction, the maximum charge separation is at the beginning of the reaction, while the minimum at the TS leading to the lowering of the energy barrier.

These results show that the mechanism of the activation of allene by the Au(I) species is very subtle, and small differences in the alcohol orientation may affect the reaction mechanism.

■ COMPUTATIONAL METHOD

The Unified Reaction Valley Approach (URVA) has been extensively described in ref 38; therefore, in the following, only a short introduction is given.

URVA monitors the mechanistic changes of an N atomic reaction complex taking place during the reaction in (3N-L)-dimensional configuration space (L: number of rotations and translations; 6 for nonlinear, 5 for linear molecule), which is decomposed into the one-dimensional (1D) reaction path space defining the valley floor and the (3N-L-1)-dimensional reaction valley being defined by the harmonic vibrational modes orthogonal to the large amplitude mode along the reaction path.[52,53]

The reaction path, $\tilde{\mathbf{x}}(s)$, is chosen as the steepest descent path in mass-weighted Cartesian coordinates in connection to the Fukui's path[54] described at each path point s according to

$$ds^2 = d\mathbf{x}^\dagger \mathbf{M}\, d\mathbf{x} \tag{1}$$

where $\mathbf{M}$ is the diagonal matrix of nuclear masses. The direction of the reaction path $\tilde{\mathbf{x}}(s)$ is defined by the unit vector $\boldsymbol{\eta}(s)$ identical with the normalized energy gradient vector $\tilde{\mathbf{g}}(s)/c(s)$ in mass-weighted Cartesian coordinates:

$$\boldsymbol{\eta}(s) = \frac{d\tilde{\mathbf{x}}(s)}{ds} = -\frac{\tilde{\mathbf{g}}(\tilde{\mathbf{x}}(s))}{c(s)} \tag{2}$$

where the normalization constant $c(s)$ is equal to the length $\|\tilde{\mathbf{g}}(s)\|$ of the gradient vector. The curvature vector $\boldsymbol{\kappa}(s)$ (orthogonal to $\boldsymbol{\eta}(s)$) is given by

$$\boldsymbol{\kappa}(s) = \frac{d^2\tilde{\mathbf{x}}(s)}{ds^2} = \frac{d\boldsymbol{\eta}(s)}{ds} = -\frac{1}{\|\tilde{\mathbf{g}}(s)\|}(\tilde{\mathbf{f}}^x(s)\boldsymbol{\eta}(s) - [(\boldsymbol{\eta}(s))^\dagger \tilde{\mathbf{f}}^x(s)\boldsymbol{\eta}(s)]\boldsymbol{\eta}(s)) \tag{3}$$

with the mass-weighted force constants matrix $\tilde{\mathbf{f}}^x(s)$.

URVA monitors each change in the curvature $\boldsymbol{\kappa}(s)$ by the decomposition of the scalar curvature $\kappa(s) = \|\boldsymbol{\kappa}(s)\|$ in terms of local internal coordinate components, where all significant chemical events are reflected by the maxima of $\kappa(s)$.[38]

The curvature maxima (K1, K2, ..., K*n*) indicate the valley region with distinct electronic structure changes, including the bond-forming and breaking events; however, the curvature minima (M1, M2, ..., M*n*; indicated by dashed vertical lines in the curvature diagrams) indicate the lower activity of the reaction complex, e.g., switching from one mechanistic event to the next. Each chemical reaction passes through a different number of chemical phases, i.e., no two chemical reactions will have the same curvature patterns, even if the reaction complex has the same number of atoms. Therefore, curvature patterns are commonly used as the fingerprints of the chemical reactions. The reaction path curvature is further decomposed in order to monitor the changes in the geometry, energy, charge transfer.[41,45] URVA has been successfully applied to a number of chemical systems,[55−61] including [3,3]-sigmatropic rearrangement of allyl acetate,[37] β-elimination reactions,[62] 1,3-dipole cycloaddition reactions to ethene and acetylene,[63,64] the isomerization of $C(BH)_2$,[65] the Diels−Alder reaction,[66] the Claisen rearrangement of chorismate,[44] to the ring-closure reactions of heptatetraene derivatives,[67] and Borane-Alane catalyzed H_2 release from water.[61]

In addition to important information about electronic and mechanical changes during chemical reactions, vibrational spectroscopy can also be used to describe the intrinsic strength of chemical bonds. Normal modes are not suited as bond strength descriptors because of the electronic and kinematic coupling between vibrational modes.[46] Therefore, the Konkoli−Cremer method (local mode analysis) was introduced to convert the normal vibrational modes into their local equivalents.[68−71] This method makes use of a mass-decoupled analogue of Wilson equation[72] of vibrational spectroscopy to solve mass coupling between normal vibrational modes. In particular, local mode bond stretching force constants k^a provides a quantitative and reliable measure of the intrinsic bond strength.[46,71] The local mode analysis has been reported as an efficient tool to derive a quantitative bond strength measure.[50,73−79] A comprehensive review is presented in ref 46. The analysis of the intrinsic bond strength by the local stretching force constant was used to describe the bond at all stationary points of the reactions **R1−R4**. Using the generalized Badger's rule,[80] the local force constant can be converted to the bond strength order (BSO*n*) through the following power relationship:

$$\mathrm{BSO}n = A(k^a)^B \tag{4}$$

The constants A and B were determined for each of the bond set by two reference molecules: (i) CC bonds: $A = 0.294$, $B = 0.825$ calculated by using $CH_3{-}CH_3$ and $CH_2{=}CH_2$ as the reference molecules with k^a(C−C) = 4.399 and k^a(C═C) = 10.187 mdyn/Å, respectively. (ii) CO bonds: $A = 0.309$, $B = 0.704$ using $CH_3{-}OH$ and $CH_2{=}O$ with k^a(C−O) = 5.288 and k^a(C═O) = 14.146 mdyn/Å, respectively. (iii) Au(I)−C bonds: $A = 0.802$, $B = 0.563$ using Au−CH_3 and Pt═CH_2 with k^a(Au−C) = 1.478 and k^a(Au═C) = 5.056 mdyn/Å, respectively. In all cases, the single bonds were assumed to have BSO*n* = 1, double bonds BSO*n* = 2, and the requirement for the zero-force constant was made BSO*n* = 0. For details, see the section on Bond Strength Orders and Table S2 in the Supporting Information.

In this work, URVA, local mode analysis, topological analysis of the electron density, and the natural bond orbital (NBO) analysis were carried out with density functional theory (DFT) using the PBE0 exchange-correlation functional.[81] The Stuggard−Dresden effective core potential (SDD)[82] was used for Au and Pople's 6-31G(d,p) basis set[83,84] for C, H, O, N atoms. The PBE0 functional was reported as an effective choice for geometry optimization of the Au-complexes[85−87] and combined with SDD is a reasonable choice to achieve high accuracy.[88] As the reaction path, the intrinsic reaction coordinates path (IRC) of Fukui[54] was used together with the improved path following the procedure of Hratchian and Kraka.[89] IRC calculations were performed using an ultrafine grid[90] and a tight convergence criterion with a step size of s = 0.03 amu$^{1/2}$ Bohr. Single point energy calculations for all stationary points were performed with the DLPNO−CCSD(T) level of theory using DFT geometries, utilizing def2-QZVPP/C for Au and def2-QZVPP basis set for all other atoms. DLPNO−CCSD(T) enthalpies and Gibbs free energies were based on the DFT thermochemistry. URVA was carried out with pURVA program[91] and the local mode analysis with the LModeA program.[92] All DFT calculations were performed with Gaussian09[93] and DLPNO−CCSD(T) with the ORCA 4.0.1 program.[94] The electron density analysis was performed with AIMALL ver. 17.11.14,[95] while NBO analysis was calculated with the NBO 6.0 program.[96]

■ ASSOCIATED CONTENT

Supporting Information

The Supporting Information is available free of charge at https://pubs.acs.org/doi/10.1021/acs.joc.1c00208.

Characterization data for all reactions including vibrational data, full energy and curvature profiles, NBO charges, and coordinates for stationary points (PDF)

Supporting videos showing the evaluation of the reaction complexes along the reaction path (ZIP)

■ AUTHOR INFORMATION

Corresponding Author

Elfi Kraka − *Computational and Theoretical Chemistry Group (CATCO), Department of Chemistry, Southern Methodist University, Dallas, Texas 75275-0314, United States;* orcid.org/0000-0002-9658-5626; Email: ekraka@gmail.com

Authors

Małgorzata Z. Makoś − *Computational and Theoretical Chemistry Group (CATCO), Department of Chemistry, Southern Methodist University, Dallas, Texas 75275-0314, United States*

Marek Freindorf − *Computational and Theoretical Chemistry Group (CATCO), Department of Chemistry, Southern Methodist University, Dallas, Texas 75275-0314, United States*

Yunwen Tao − *Computational and Theoretical Chemistry Group (CATCO), Department of Chemistry, Southern Methodist University, Dallas, Texas 75275-0314, United States*

Complete contact information is available at: https://pubs.acs.org/10.1021/acs.joc.1c00208

Notes

The authors declare no competing financial interest.

■ ACKNOWLEDGMENTS

The authors thank SMU for providing excellent computational resources. This work was supported by the National Science Foundation, Grant CHE 1464906.

■ REFERENCES

(1) Mora, M.; Gimeno, M. C.; Visbal, R. Recent Advances in Gold-NHC Complexes with Biological Properties. *Chem. Soc. Rev.* **2019**, *48*, 447−462.

(2) Wurm, T.; Asiri, A. M.; Hashmi, A. S. K. *N-Heterocyclic Carbenes*; Wiley-VCH Verlag GmbH & Co. KGaA, 2014; pp 243−270.

(3) Karaaslan, M. G.; Aktaş, A.; Gürses, C.; Gök, Y.; Ateş, B. Chemistry, Structure, and Biological Roles of Au-NHC Complexes as TrxR Inhibitors. *Bioorg. Chem.* **2020**, *95*, 103552.

(4) Scattolin, T.; Nolan, S. P. Synthetic Routes to Late Transition Metal−NHC Complexes. *Trends Chem.* **2020**, *2*, 721−736.

(5) Jalal, M.; Hammouti, B.; Touzani, R.; Aouniti, A.; Ozdemir, I. Metal-NHC Heterocycle Complexes in Catalysis and Biological Applications: Systematic Review. *Mater. Today Proc.* **2020**, *31*, S122−S129.

(6) Marion, N.; Gealageas, R.; Nolan, S. P. [(NHC)AuI]-Catalyzed Rearrangement of Allylic Acetates. *Org. Lett.* **2007**, *9*, 2653−2656.

(7) Fürstner, A.; Davies, P. W. Catalytic Carbophilic Activation: Catalysis by Platinum and Gold n Acids. *Angew. Chem., Int. Ed.* **2007**, *46*, 3410−3449.

(8) Fernández, G. A.; Dorn, V.; Chopa, A. B.; Silbestri, G. F. Steric Hindrance and Electronic Effects of Sulfonatepropyl Chain on Gold Center. An Experimental and DFT Study. *J. Organomet. Chem.* **2017**, *852*, 20−26.

(9) Hopkinson, M. N.; Richter, C.; Schedler, M.; Glorius, F. An Overview of N-heterocyclic Carbenes. *Nature* **2014**, *510*, 485−496.

(10) Marion, N.; Díez-González, S.; Nolan, S. P. N-Heterocyclic Carbenes as Organocatalysts. *Angew. Chem., Int. Ed.* **2007**, *46*, 2988−3000.

(11) Glorius, F. *N-Heterocyclic Carbenes in Transition Metal Catalysis*; Springer Berlin Heidelberg, 2007.

(12) Lu, Z.; Hammond, G. B.; Xu, B. Improving Homogeneous Cationic Gold Catalysis through a Mechanism-Based Approach. *Acc. Chem. Res.* **2019**, *52*, 1275−1288.

(13) Hashmi, A. S. K. Gold-Catalyzed Organic Reactions. *Chem. Rev.* **2007**, *107*, 3180−3211.

(14) Schießl, J.; Schulmeister, J.; Doppiu, A.; Wörner, E.; Rudolph, M.; Karch, R.; Hashmi, A. S. K. An Industrial Perspective on Counter Anions in Gold Catalysis: Underestimated with Respect to "Ligand Effects. *Adv. Synth. Catal.* **2018**, *360*, 2493−2502.

(15) Jiménez-Núñez, E.; Echavarren, A. M. Molecular Diversity Through Gold Catalysis with Alkynes. *Chem. Commun.* **2007**, 333−346.

(16) Quintavalla, A.; Bandini, M. Gold-Catalyzed Allylation Reactions. *ChemCatChem* **2016**, *8*, 1437−1453.

(17) Lim, W.; Kim, J.; Rhee, Y. H. Pd-Catalyzed Asymmetric Intermolecular Hydroalkoxylation of Allene: An Entry to Cyclic Acetals with Activating Group-Free and Flexible Anomeric Control. *J. Am. Chem. Soc.* **2014**, *136*, 13618−13621.

(18) Pérez-Mayoral, E.; Matos, I.; Nachtigall, P.; Položij, M.; Fonseca, I.; Vitvarová-Procházková, D.; Čejka, J. Intramolecular Hydroalkoxylation of Non-Activated C═C Bonds Catalysed by Zeolites: An Experimental and Theoretical Study. *ChemSusChem* **2013**, *6*, 1021−1030.

(19) Soklou, K. E.; Marzag, H.; Bouillon, J.-P.; Marchivie, M.; Routier, S.; Plé, K. Gold(I)-Catalyzed Intramolecular Hydroamination and Hydroalkoxylation of Alkynes: Access to Original Heterospirocycles. *Org. Lett.* **2020**, *22*, 5973−5977.

(20) Huang, X.; Ma, S. Allenation of Terminal Alkynes with Aldehydes and Ketones. *Acc. Chem. Res.* **2019**, *52*, 1301−1312.

(21) Yu, S.; Ma, S. Allenes in Catalytic Asymmetric Synthesis and Natural Product Syntheses. *Angew. Chem., Int. Ed.* **2012**, *51*, 3074−3112.

(22) Soriano, E.; Fernández, I. Allenes and Computational Chemistry: From Bonding Situations to Reaction Mechanisms. *Chem. Soc. Rev.* **2014**, *43*, 3041.

(23) Zhang, Z.; Widenhoefer, R. A. Regio- And Stereoselective Synthesis of Alkyl Allylic Ethers via Gold(I)-Catalyzed Intermodular Hydroalkoxylation of Allenes with Alcohols. *Org. Lett.* **2008**, *10*, 2079−2081.

(24) Harris, R. J.; Carden, R. G.; Duncan, A. N.; Widenhoefer, R. A. Kinetics and Mechanism of the Gold-Catalyzed Intermolecular Hydroalkoxylation of Allenes with Alcohols. *ACS Catal.* **2018**, *8*, 8941−8952.

(25) Paton, R. S.; Maseras, F. Gold (I) -Catalyzed Intermolecular Hydroalkoxylation of Allenes: a DFT study. *Org. Lett.* **2009**, *11*, 2237−2240.

(26) Batuecas, M.; Castro-Rodrigo, R.; Esteruelas, M. A.; García-Yebra, C.; López, A. M.; Oñate, E. Aromatic Osmacyclopropenefuran Bicycles and Their Relevance for the Metal-Mediated Hydration of Functionalized Allenes. *Angew. Chem., Int. Ed.* **2016**, *55*, 13749−13753.

(27) Muñoz-López, S.; Couce-Rios, A.; Sciortino, G.; Lledós, A.; Ujaque, G. Mechanistic Insights on the Hydration of Terminal and Internal Allenes Catalyzed by $[(NHC)Au]^+$. *Organometallics* **2018**, *37*, 3543−3551.

(28) Wang, Z. J.; Benitez, D.; Tkatchouk, E.; W, A. G., III; Toste, F. D. Mechanistic Study of Gold(I)-Catalyzed Intermolecular Hydroamination of Allenes. *J. Am. Chem. Soc.* **2010**, *132*, 13064−13071.

(29) Kinjo, R.; Donnadieu, B.; Bertrand, G. Gold-Catalyzed Hydroamination of Alkynes and Allenes with Parent Hydrazine. *Angew. Chem., Int. Ed.* **2011**, *50*, 5560−5563.

(30) El-Sepelgy, O.; Brzozowska, A.; Sklyaruk, J.; Jang, Y. K.; Zubar, V.; Rueping, M. Cooperative Metal−Ligand Catalyzed Intramolecular Hydroamination and Hydroalkoxylation of Allenes Using a Stable Iron Catalyst. *Org. Lett.* **2018**, *20*, 696−699.

(31) Mascareñas, J. L.; Varela, I.; López, F. Allenes and Derivatives in Gold(I)- and Platinum(II)-Catalyzed Formal Cycloadditions. *Acc. Chem. Res.* **2019**, *52*, 465−479.

(32) Zhao, F.; Lv, K.; Liu, T. Computational Study on the Mechanisms of [2 + 3] and [2 + 2] Cycloisomerization Reaction Catalyzed by Gold Complex. *J. Organomet. Chem.* **2018**, *874*, 63−69.

(33) Shahzad, S. A.; Sajid, M. A.; Khan, Z. A.; Canseco-Gonzalez, D. Gold Catalysis in Organic Transformations: A Review. *Synth. Commun.* **2017**, *47*, 735−755.

(34) Basak, A.; Chakrabarty, K.; Ghosh, A.; Das, G. K. Theoretical Study on the Isomerization of Propargyl Derivative to Conjugated Diene Under Au(I)-Catalyzed Reaction: A DFT Study. *Comput. Theor. Chem.* **2016**, *1083*, 38−45.

(35) Zi, W.; Toste, F. D. Recent Advances in Enantioselective Gold Catalysis. *Chem. Soc. Rev.* **2016**, *45*, 4567−4589.

(36) Ishida, T.; Koga, H.; Okumura, M.; Haruta, M. Advances in Gold Catalysis and Understanding the Catalytic Mechanism. *Chem. Rec.* **2016**, *16*, 2278−2293.

(37) Freindorf, M.; Cremer, D.; Kraka, E. Gold(I)-Assisted Catalysis - A Comprehensive View on the [3,3]-Sigmatropic Rearrangement of Allyl Acetate. *Mol. Phys.* **2018**, *116*, 611−630.

(38) Kraka, E.; Zou, W.; Tao, Y.; Freindorf, M. Exploring the Mechanism of Catalysis with the Unified Reaction Valley Approach (URVA) - A Review. *Catalysts* **2020**, *10*, 691.

(39) Zou, W.; Sexton, T.; Kraka, E.; Freindorf, M.; Cremer, D. A New Method for Describing the Mechanism of a Chemical Reaction Based on the Unified Reaction Valley Approach. *J. Chem. Theory Comput.* **2016**, *12*, 650−663.

(40) Kraka, E. Reaction Path Hamiltonian and the Unified Reaction Valley Approach. *WIREs: Comput. Mol. Sci.* **2011**, *1*, 531−556.

(41) Kraka, E.; Cremer, D. Computational Analysis of the Mechanism of Chemical Reactions in Terms of Reaction Phases: Hidden Intermediates and Hidden Transition States. *Acc. Chem. Res.* **2010**, *43*, 591−601.

(42) Alonso, J. M.; Muñoz, M. P. Platinum and Gold Catalysis: à la Carte Hydroamination of Terminal Activated Allenes with Azoles. *Org. Lett.* **2019**, *21*, 7639−7644.

(43) Cohen, A. J.; Mori-Sánchez, P.; Yang, W. Challenges for Density Functional Theory. *Chem. Rev.* **2012**, *112*, 289−320.

(44) Freindorf, M.; Tao, Y.; Sethio, D.; Cremer, D.; Kraka, E. New Mechanistic Insights into the Claisen Rearrangement of Chorismate - A Unified Reaction Valley Approach Study. *Mol. Phys.* **2019**, *117*, 1172−1192.

(45) Cremer, D.; Kraka, E. From Molecular Vibrations to Bonding, Chemical Reactions, and Reaction Mechanism. *Curr. Org. Chem.* **2010**, *14*, 1524−1560.

(46) Kraka, E.; Zou, W.; Tao, Y. Decoding Chemical Information from Vibrational Spectroscopy Data: Local Vibrational Mode Theory. *WIREs: Comput. Mol. Sci.* **2020**, *10*, 1480.

(47) Bader, R. F. W. *Atoms in Molecules—A Quantum Theory*; Oxford University Press: Oxford, UK, 1990.

(48) Cremer, D.; Kraka, E. A Description of the Chemical Bond in Terms of Local Properties of Electron Density and Energy. *Croatica Chem. Acta* **1984**, *57*, 1259−1281.

(49) Kraka, E.; Cremer, D. *Theoretical Models of Chemical Bonding. The Concept of the Chemical Bond*; Maksic, Z.B., Ed.; Springer Verlag: Heidelberg, 1990; Vol. 2, p 453.

(50) Makoś, M. Z.; Freindorf, M.; Sethio, D.; Kraka, E. New Insights into Fe−H_2 and Fe−H^- Bonding of a [NiFe] Hydrogenase Mimic − A Local Vibrational Mode Study. *Theor. Chem. Acc.* **2019**, *138*, 76.

(51) Nanayakkara, S.; Kraka, E. A New Way of Studying Chemical Reactions: A Hand-in-hand URVA and QTAIM Approach. *Phys. Chem. Chem. Phys.* **2019**, *21*, 15007−15018.

(52) Miller, W. H.; Handy, N. C.; Adams, J. E. Reaction Path Hamiltonian for Polyatomic Molecules. *J. Chem. Phys.* **1980**, *72*, 99−112.

(53) Kato, S.; Morokuma, K. Potential energy characteristics and energy partitioning in chemical reactions: Ab initio MO study of four-centered elimination reaction CH_3CH_2F − > CH_2=CH_2 + HF. *J. Chem. Phys.* **1980**, *73*, 3900−3914.

(54) Fukui, K. The Path of Chemical Reactions - the IRC Approach. *Acc. Chem. Res.* **1981**, *14*, 363−368.

(55) Konkoli, Z.; Kraka, E.; Cremer, D. Unified Reaction Valley Approach Mechanism of the Reaction $CH_3 + H_2 \rightarrow CH_4$ + H. *J. Phys. Chem. A* **1997**, *101*, 1742−1757.

(56) Cremer, D.; Wu, A.; Kraka, E. The Mechanism of the Reaction FH + $H_2C = CH_2 \rightarrow H_2C - CFH_3$. Investigation of Hidden Intermediates with the Unified Reaction Valley Approach. *Phys. Chem. Chem. Phys.* **2001**, *3*, 674−687.

(57) Kraka, E.; Wu, A.; Cremer, D. Mechanism of the Diels-Alder Reaction Studied with the United Reaction Valley Approach: Mechanistic Differences between Symmetry-Allowed and Symmetry-Forbidden Reactions. *J. Phys. Chem. A* **2003**, *107*, 9008−9021.

(58) Joo, H.; Kraka, E.; Quapp, W.; Cremer, D. The Mechanism of a Barrierless Reaction: Hidden Transition State and Hidden Intermediates in the Reaction of Methylene with Ethene. *Mol. Phys.* **2007**, *105*, 2697−2717.

(59) Kraka, E.; Zou, W.; Freindorf, M.; Cremer, D. Energetics and Mechanism of the Hydrogenation of XH_n for Group IV to Group VII Elements X. *J. Chem. Theory Comput.* **2012**, *8*, 4931−4943.

(60) Kraka, E.; Joo, H.; Cremer, D. A Stunning Example for a Spontaneous Reaction with a Complex Mechanism: The Vinylidene-Acetylene Cycloaddition Reaction. *Mol. Phys.* **2010**, *108*, 2667−2685.

(61) Nanayakkara, S.; Freindorf, M.; Tao, Y.; Kraka, E. Modeling Hydrogen release from water with Borane and Alane catalysts: A Unified Reaction Valley Approach. *J. Phys. Chem. A* **2020**, *124*, 8978−8993.

(62) Reis, M. C.; López, C. S.; Kraka, E.; Cremer, D.; Faza, O. N. Rational Design in Catalysis: A Mechanistic Study of β-Hydride Eliminations in Gold(I) and Gold(III) Complexes Based on Features of the Reaction Valley. *Inorg. Chem.* **2016**, *55*, 8636−8645.

(63) Freindorf, M.; Sexton, T.; Kraka, E.; Cremer, D. The Mechanism of the Cycloaddition Reaction of 1,3-Dipole Molecules with Acetylene - An Investigation with the Unified Reaction Valley Approach. *Theor. Chem. Acc.* **2014**, *133*, 1423.

(64) Sexton, T. M.; Freindorf, M.; Kraka, E.; Cremer, D. A Reaction Valley Investigation of the Cycloaddition of 1,3-Dipoles with the Dipolarophiles Ethene and Acetylene: Solution of a Mechanistic Puzzle. *J. Phys. Chem. A* **2016**, *120*, 8400−8418.

(65) Barua, S. R.; Allen, W. D.; Kraka, E.; Jerabek, P.; Sure, R.; Frenking, G. Nearly Degenerate Isomers of $C(BH)_2$: Cumulene, Carbene, or Carbone? *Chem. - Eur. J.* **2013**, *19*, 15941−15954.

(66) Sexton, T.; Kraka, E.; Cremer, D. Extraordinary Mechanism of the Diels-Alder Reaction: Investigation of Stereochemistry, Charge

Transfer, Charge Polarization, and Biradicaloid Formation. *J. Phys. Chem. A* **2016**, *120*, 1097−1111.

(67) López, C. S.; Faza, O. N.; Freindorf, M.; Kraka, E.; Cremer, D. Solving the Pericyclic-Pseudo pericyclic Puzzle in the Ring-Closure Reactions of 1,2,4,6-Heptatetraene Derivatives. *J. Org. Chem.* **2016**, *81*, 404−414.

(68) Konkoli, Z.; Cremer, D. A New Way of Analyzing Vibrational Spectra. I. Derivation of Adiabatic Internal Modes. *Int. J. Quantum Chem.* **1998**, *67*, 1−9.

(69) Zou, W.; Kalescky, R.; Kraka, E.; Cremer, D. Relating Normal Vibrational Modes to Local Vibrational Modes with the Help of an Adiabatic Connection Scheme. *J. Chem. Phys.* **2012**, *137*, 084114.

(70) Zou, W.; Cremer, D. Properties of Local Vibrational Modes: The Infrared Intensity. *Theor. Chem. Acc.* **2014**, *133*, 1451−1466.

(71) Zou, W.; Cremer, D. C_2 in a Box: Determining its Intrinsic Bond Strength for the $X^1\ \Sigma^+{}_g$ Ground State. *Chem. - Eur. J.* **2016**, *22*, 4087−4097.

(72) Wilson, E. B.; Decius, J. C.; Cross, P. C. M. *Molecular Vibrations. The Theory of Infrared and Raman Vibrational Spectra*; McGraw-Hill: New York, 1955; pp 59−136.

(73) Yannacone, S.; Oliveira, V.; Verma, N.; Kraka, E. A Continuum from Halogen Bonds to Covalent Bonds: Where Do λ^3 Iodanes Fit? *Inorganics* **2019**, *7*, 47.

(74) Oliveira, V. P.; Kraka, E.; Machado, F. B. C. Pushing 3c-4e Bonds to the Limit: A Coupled Cluster Study of Stepwise Fluorination of First-Row Atoms. *Inorg. Chem.* **2019**, *58*, 14777−14789.

(75) Lefton, J.; Pekar, K.; Sethio, D.; Kraka, E.; Runčevski, T. Crystal Structure of 1-propanethiol − Co2(dobdc) from Laboratory X-ray Powder Diffraction Data. *Powder Diffraction* **2020**, *35*, 1−6.

(76) Zou, W.; Tao, Y.; Freindorf, M.; Cremer, D.; Kraka, E. Local Vibrational Force Constants - from the Assessment of Empirical Force Constants to the Description of Bonding in Large Systems. *Chem. Phys. Lett.* **2020**, *748*, 137337.

(77) Makoś, M. Z.; Zou, W.; Freindorf, M.; Kraka, E. Metal-Ring Interactions in Actinide Sandwich Compounds: A Combined Normalized Elimination of the Small Component and Local Vibrational Mode Study. *Mol. Phys.* **2020**, *118*, No. e1768314.

(78) Tao, Y.; Zhang, L.; Zou, W.; Kraka, E. Equilibrium Geometries, Adiabatic Excitation Energies and Intrinsic C═C/C-H Bond Strengths of Ethylene in Lowest Singlet Excited States Described by TDDFT. *Symmetry* **2020**, *12*, 1545.

(79) Delgado, A. A. A.; Sethio, D.; Munar, I.; Aviyente, V.; Kraka, E. Local Vibrational Mode Analysis of Ion−Solvent and Solvent−Solvent Interactions for Hydrated Ca^{2+} Clusters. *J. Chem. Phys.* **2020**, *153*, 224303.

(80) Kraka, E.; Larsson, J. A.; Cremer, D. In *Computational Spectroscopy*; Grunenberg, J., Ed.; Wiley: New York, 2010; pp 105−149.

(81) Adamo, C.; Barone, V. Toward reliable density functional methods without adjustable parameters: The PBE0 model. *J. Chem. Phys.* **1999**, *110*, 6158−6170.

(82) Schwerdtfeger, P.; Dolg, M.; Schwarz, W. H. E.; Bowmaker, G. A.; Boyd, P. D. W. Relativistic Effects in Gold Chemistry. I. Diatomic Gold Compounds. *J. Chem. Phys.* **1989**, *91*, 1762−1774.

(83) Ditchfield, R.; Hehre, W. J.; Pople, J. A. Self-Consistent Molecular-Orbital Methods. IX. An Extended Gaussian-Type Basis for Molecular-Orbital Studies of Organic Molecules. *J. Chem. Phys.* **1971**, *54*, 724−728.

(84) Hariharan, P. C.; Pople, J. A. The Influence of Polarization Functions on Molecular Orbital Hydrogenation Energies. *Theoret. Chim. Acta* **1973**, *28*, 213−222.

(85) Bühl, M.; Reimann, C.; Pantazis, D. A.; Bredow, T.; Neese, F. Geometries of Third-Row Transition-Metal Complexes from Density-Functional Theory. *J. Chem. Theory Comput.* **2008**, *4*, 1449−1459.

(86) Kang, R.; Chen, H.; Shaik, S.; Yao, J. Assessment of Theoretical Methods for Complexes of Gold(I) and Gold(III) with Unsaturated Aliphatic Hydrocarbon: Which Density Functional Should We Choose? *J. Chem. Theory Comput.* **2011**, *7*, 4002−4011.

(87) Muniz-Miranda, F.; Menziani, M. C.; Pedone, A. Assessment of Exchange-Correlation Functionals in Reproducing the Structure and Optical Gap of Organic-Protected Gold Nanoclusters. *J. Phys. Chem. C* **2014**, *118*, 7532−7544.

(88) Faza, O. N.; López, C. S. *Topics in Current Chemistry*; Springer International Publishing, 2014; pp 213−283.

(89) Hratchian, H. P.; Kraka, E. Improved Predictor-Corrector Integrators For Evaluating Reaction Path Curvature. *J. Chem. Theory Comput.* **2013**, *9*, 1481−1488.

(90) Gräfenstein, J.; Cremer, D. Efficient DFT integrations by locally augmented radial grids. *J. Chem. Phys.* **2007**, *127*, 164113.

(91) Tao, Y.; Zou, W.; Freindorf, M.; Cremer, D.; Kraka, E. *pURVA*; Southern Methodist University: Dallas, TX, 2020.

(92) Zou, W.; Tao, Y.; Freindorf, M.; Makoś, M. Z.; Verma, N.; Kraka, E. *LModeA Program*; Southern Methodist University: Dallas, TX, 2020.

(93) Frisch, M. J. et al. *Gaussian 09*, Revision D.01; Gaussian Inc.: Wallingford, CT, 2013.

(94) Neese, F. The ORCA program system. *Wiley Interdiscip. Rev.: Comput. Mol. Sci.* **2012**, *2*, 73−78.

(95) Keith, T. A. *AIMAll*, Version 17.11.14; K Gristmill Software: Overland Park, KS, 2017. aim.tkgristmill.com.

(96) Weinhold, F.; Landis, C. R. *Valency and Bonding: A Natural Bond Orbital Donor-Acceptor Perspective*; Cambridge University Press and Theoretical Chemistry Institute, University of Wisconsin: Cambridge, U.K. and Madison, WI, 2003.